AIMS Mathematics, 11(11): 36356–36378.
DOI: 10.3934/math.20261407
Received: 05 September 2026
Revised: 20 October 2026
Accepted: 26 October 2026
Published: 04 November 2026

https://www.aimspress.com/journal/Math

Research article

Long-transient behaviors and dynamical misjudgment in a Filippov piecewise-smooth population model

Zheqi Tao[1], Yi Yang[2,*] and Changcheng Xiang[3]

[1] School of Mathematics and Statistics, Chongqing Sanxia University of Science and Technology, Chongqing, 404120, China

[2] School of Computer Science and Engineering, Chongqing Sanxia University of Science and Technology, Chongqing, 404120, China

[3] School of Mathematics and Statistics, Hubei Minzu University, Enshi, 445000, China

* **Correspondence:** Email: yang1595@126.com.

Abstract: We developed a three-dimensional Filippov piecewise-smooth population system characterizing aphid–ladybug–ant interactions, in which a threshold-based switching function describes the transition of aphids between pure reproduction and honeydew-excreting ant-recruitment strategies. In conventional numerical simulations of ecological models, sustained oscillations are often identified directly as steady-state limit cycles. Within the framework of non-smooth dynamical systems, the sliding dynamics, equilibrium classification, and stability of the model were analyzed. Time-series simulations, maximum Lyapunov exponent scans, and semi-logarithmic amplitude-decay analysis revealed that the long-lasting damped oscillations of the system are long transients rather than genuine limit cycles, which can be easily misjudged as steady-state oscillations under finite simulation time. The system exhibited monostable and bistable behaviors within the parameter domains examined, and the long transients were jointly induced by the weak stability of equilibria and the geometric constraints of the piecewise switching structure; the threshold switching, rather than any adaptive optimization, shaped the transient population dynamics. These findings highlight the distinction between transient evolution and genuine steady-state behavior in threshold-regulated ecosystems and provide reliable references for the numerical identification of such dynamics.

Keywords: Filippov system; long transient; predation-mutualism; bistability; population dynamics
Mathematics Subject Classification: 34A36, 37G35

1. Introduction

The aphid–ladybug–ant system represents a typical predation-mutualism coupled ecosystem in nature [1, 2]. Aphids feed on plant sap for reproduction, yet they lack effective defensive mechanisms and are vulnerable to predation by ladybugs [3]. Aphids can secrete honeydew to attract ants [4]. While feeding on honeydew, ants drive away ladybugs and provide protection for aphids. Nevertheless, honeydew secretion consumes aphids' energy and inhibits aphid population reproduction. Accordingly, aphids balance benefits against costs according to the level of natural enemy threat, switching between "full-scale reproduction" and "recruiting ants for defence at metabolic cost". Such a strategic choice means that the population dynamics no longer follow a single smooth system of ordinary differential equations, thereby forming a Filippov piecewise-smooth system. In this paper, a Filippov piecewise-smooth dynamical model is established for aphids x, ladybugs y_n, and ants y_m:

$$\begin{cases} \dfrac{dx}{dt} = rx\left(1 - \dfrac{x}{K}\right) - \dfrac{a_n x y_n}{1 + bx} - cxy_n, \\ \dfrac{dy_n}{dt} = \dfrac{\eta_1 a_n x y_n}{1 + bx} - \mu_n y_n - \delta y_m y_n, \\ \dfrac{dy_m}{dt} = -\mu_m y_m + \eta_2 \alpha x y_n, \end{cases} \tag{1.1}$$

with

$$\begin{cases} \delta, c, \eta_2 = 0, \quad H(x, y_n, y_m) < 0, \\ \delta, c, \eta_2 > 0, \quad H(x, y_n, y_m) > 0. \end{cases}$$

$H(x, y_n, y_m) = y_n - \beta y_m - \gamma$, α denotes the honeydew secretion rate of aphids, η_2 represents the conversion efficiency from honeydew to the ant population, a_n is the attack rate of ladybugs in the absence of ants, b is the half-saturation constant of the Holling type–II predation term, η_1 is the conversion efficiency of ladybugs, μ_m is the natural mortality rate of ants, μ_n is the natural mortality rate of ladybugs, δ characterizes the interference effect of ants on ladybugs; c stands for the reproduction cost incurred by aphids for honeydew secretion, β describes the protective strength provided by ants; γ is the critical threat threshold of ladybugs, r is the intrinsic growth rate of aphids, and K is the environmental carrying capacity.

The Filippov piecewise-smooth system exhibits rich dynamical behaviors including sliding motion and coexistence of multiple attractors [5, 6]. Recent studies have further extended threshold-control Filippov modeling to reaction–diffusion and multi-trophic settings; for instance, Zhang and Yang analyzed a reaction–diffusion Filippov food-chain model with threshold control and systematically examined the interplay between diffusion-induced dynamics and the sliding modes generated by threshold switching [7]. Most existing studies on aphid–ladybug–ant interactions rely on numerical simulations to analyze population oscillations, and frequently interpret sustained oscillations observed in simulations directly as stable limit cycles [8]. Nevertheless, long-transient effects exist in piecewise-smooth systems: trajectories can display oscillatory time-series characteristics over an extended period and converge to equilibrium points only after extremely long evolution [9]. If the simulation duration is insufficient, long-transient oscillations can be easily confused with genuine steady-state self-sustained oscillations, leading to dynamical misjudgment [10].

To address the above-mentioned issues, this paper adopts the Filippov piecewise-smooth ecological model given by system (1.1). Combined with time-series simulation and phase-plane analysis, it

illustrates the dilemma of dynamical identification caused by insufficient simulation duration. By means of parameter scanning of the maximum Lyapunov exponent [11], quantitative semi-logarithmic amplitude-decay analysis [12], and linearization of the Jacobian matrix at equilibrium points, this study distinguishes long-transient oscillations [13] from steady-state attractors [14] and reveals the intrinsic mechanism behind the emergence of long transients. The obtained results can provide theoretical references for interpreting numerical simulations of piecewise ecological systems with strategy-switching behaviors.

The organization of this paper is outlined as follows. Section 2 introduces the basic properties and dynamical descriptions of the two subsystems within the Filippov system. Section 3 explores the sliding-mode characteristics of the sliding vector field, identifies all possible equilibrium points, and the corresponding dynamical behaviors. Section 4 carries out dynamical simulations and quantitative analyzes to recognize long-transient behaviors and reveal their formation mechanisms. Section 5 summarizes and discusses the whole paper, concludes the main findings, and illustrates the ecological implications of the proposed model.

2. Model and basic properties

2.1. Filippov system

Based on the biological interpretation of the model, analysis is restricted to system (1.1) on $\mathbf{R}^3_+ = \{(x, y_n, y_m) \mid x \geq 0, y_n \geq 0, y_m \geq 0\}$. The Filippov representation of system (1.1) is written as:

$$\frac{d\mathbf{X}(t)}{dt} = \begin{cases} \mathbf{F}_{S_1}(\mathbf{X}(t)), & \mathbf{X}(t) \in S_1, \\ \mathbf{F}_{S_2}(\mathbf{X}(t)), & \mathbf{X}(t) \in S_2, \end{cases} \tag{2.1}$$

where $\mathbf{X} = (x, y_n, y_m)^T$, $S_1 = \{(x, y_n, y_m) \mid H(x, y_n, y_m) < 0\}$, $S_2 = \{(x, y_n, y_m) \mid H(x, y_n, y_m) > 0\}$, and $H(x, y_n, y_m) = y_n - \beta y_m - \gamma$ with $\gamma > 0$.

$$\mathbf{F}_{S_1}(\mathbf{X}(t)) = \left(rx(1 - \frac{x}{K}) - \frac{a_n x y_n}{1 + bx}, \frac{\eta_1 a_n x y_n}{1 + bx} - \mu_n y_n, -\mu_m y_m \right)^T,$$
$$\mathbf{F}_{S_2}(\mathbf{X}(t)) = \left(rx(1 - \frac{x}{K}) - \frac{a_n x y_n}{1 + bx} - c x y_n, \frac{\eta_1 a_n x y_n}{1 + bx} - \mu_n y_n - \delta y_m y_n, -\mu_m y_m + \eta_2 \alpha x y_n \right)^T.$$

Two modeling choices deserve a brief explanation. First, the cost of honeydew secretion is modeled by the bilinear term $-cxy_n$: the secretion effort of an individual aphid is stimulated by the presence of ladybugs, so that the per-capita reproductive cost is proportional to the ladybug density y_n, while the total cost scales with the aphid abundance x. This mass-action form is adopted, rather than a saturating one, because the saturating Holling type–II response has already been assigned to the predation term, and the bilinear cost keeps the algebraic analysis tractable (explicit equilibria and the quartic equation are solved in the Appendix); the same convention is standard in threshold-control pest models [15]. Second, the switching function $H = y_n - \beta y_m - \gamma$ does not involve the aphid density x: the defensive switch is triggered by the predation threat perceived by the aphids, which is measured by the ladybug density y_n reduced by the protection βy_m provided by ants and compared with the critical threshold γ, and this threat level does not depend on the aphids' own abundance.

The discontinuous boundary is denoted by $\Sigma = \{(x, y_n, y_m) \mid H(x, y_n, y_m) = 0\}$ [16]. This boundary separates the two regions associated with subsystems S_1 and S_2. Consequently, the state space $\mathbb{R}^3_+$ is

divided into three parts, namely, S_1, Σ, and S_2, such that $\mathbb{R}^3_+ = S_1 \cup \Sigma \cup S_2$. In this expression, the regions S_1 and S_2 of the Filippov system are referred to as subsystem S_1 and subsystem S_2, respectively.

2.2. *Dynamics of subsystem S_1*

This section focuses on the existence of nonnegative equilibrium points and the analysis of their local stability for subsystem S_1. Subsystem S_1 admits three equilibrium points within the nonnegative region:

$$E^1_{S_1} = (0, 0, 0), \qquad E^2_{S_1} = (K, 0, 0), \qquad E^3_{S_1} = (x_1, y_{n1}, 0)$$

and

$$x_1 = \frac{\mu_n}{\eta_1 a_n - \mu_n b}, \qquad y_{n1} = \frac{r(1 - x_1/K)(1 + bx_1)}{a_n}.$$

The presence of these equilibrium points indicates the following properties:

- The boundary equilibria $E^1_{S_1} = (0, 0, 0)$ and $E^2_{S_1} = (K, 0, 0)$ always occur in the system;
- The positive equilibrium $E^3_{S_1} = (x_1, y_{n1}, 0)$ exists if and only if $0 < x_1 < K$ holds. In terms of the model parameters, this two-sided condition is equivalent to $\eta_1 a_n - \mu_n b > 0$ and $\mu_n(1 + bK) < K\eta_1 a_n$: the first inequality guarantees $x_1 > 0$, while $x_1 < K$ is equivalent to the second one since $x_1 = \mu_n/(\eta_1 a_n - \mu_n b)$.

Based on the preceding discussion, the Jacobian matrix of subsystem S_1 can be written as

$$\mathbf{J}|_{E^i_{S_1}(x,y_n,y_m)} = \begin{pmatrix} r - \dfrac{2rx}{K} - \dfrac{a_n y_n}{(1+bx)^2} & -\dfrac{a_n x}{1+bx} & 0 \\ \dfrac{\eta_1 a_n y_n}{(1+bx)^2} & \dfrac{\eta_1 a_n x}{1+bx} - \mu_n & 0 \\ 0 & 0 & -\mu_m \end{pmatrix}\Bigg|_{E^i_{S_1}(x,y_n,y_m)},$$

where $i = 1, 2, 3$. Let $\lambda_j (j = 1, 2, 3)$ denote the three eigenvalues of the characteristic equation evaluated at $E^i_{S_1}$. The local stability of the equilibrium point $E^i_{S_1} = (x, y_n, y_m)$ is therefore governed by these eigenvalues. At the equilibrium point $E^1_{S_1} = (0, 0, 0)$, the characteristic equation yields eigenvalues $\lambda_1 = r$, $\lambda_2 = -\mu_n$, and $\lambda_3 = -\mu_m$, which implies that $E^1_{S_1} = (0, 0, 0)$ corresponds to an unstable saddle point.

The characteristic equation associated with $E^2_{S_1} = (K, 0, 0)$ is given by

$$(\lambda + r)(\lambda - \frac{\eta_1 a_n K}{1 + bK} + \mu_n)(\lambda + \mu_m) = 0,$$

where

$$\lambda_1 = -r, \qquad \lambda_2 = \frac{\eta_1 a_n K}{1 + bK} - \mu_n, \qquad \lambda_3 = -\mu_m.$$

Since $\lambda_1, \lambda_3 < 0$, the stability of $E^2_{S_1}$ depends on λ_2: when $\dfrac{\eta_1 a_n K}{1 + bK} < \mu_n$, the equilibrium $E^2_{S_1}$ represents a stable node. In contrast, when $\dfrac{\eta_1 a_n K}{1 + bK} > \mu_n$, $E^2_{S_1}$ becomes an unstable saddle point.

The characteristic equation related to $E^3_{S_1} = (x_1, y_{n1}, 0)$ is expressed in the form below:

$$(\lambda + \mu_m)\left[\lambda^2 - a_{11}\lambda - a_{12}a_{21}\right] = 0$$

and

$$a_{11} = r\left(1 - \frac{2x_1}{K}\right) - \frac{r\left(1 - \frac{x_1}{K}\right)}{1 + bx_1}, \quad a_{12} = -\frac{a_n x_1}{1 + bx_1}, \quad a_{21} = \frac{\eta_1 r\left(1 - \frac{x_1}{K}\right)}{1 + bx_1},$$

where

$$\lambda_1 = -\mu_m, \quad \lambda_2 = \frac{a_{11} - \sqrt{a_{11}^2 + 4a_{12}a_{21}}}{2}, \quad \lambda_3 = \frac{a_{11} + \sqrt{a_{11}^2 + 4a_{12}a_{21}}}{2}.$$

Let $C = -a_{12}a_{21} = \eta_1 a_n r x_1 (1 - x_1/K) / (1 + bx_1)^2$, and then $C > 0$. The characteristic roots can be rewritten as

$$\lambda_1 = -\mu_m, \quad \lambda_2 = \frac{a_{11} - \sqrt{a_{11}^2 - 4C}}{2}, \quad \lambda_3 = \frac{a_{11} + \sqrt{a_{11}^2 - 4C}}{2}.$$

Since $\lambda_1 = -\mu_m < 0$, the stability of $E^3_{S_1}$ depends on λ_2, λ_3. Observe that $\sqrt{a_{11}^2 - 4C} < |a_{11}|$ whenever $C > 0$; hence the sign of the real parts of λ_2, λ_3 is governed by a_{11} alone, while the sign of $a_{11}^2 - 4C$ distinguishes between node-type and focus-type behavior:

(i) if $a_{11} < 0$ and $a_{11}^2 \geq 4C$, then $\lambda_2 \leq \lambda_3 < 0$ are two (possibly coincident) negative real roots, and $E^3_{S_1}$ is a stable node;
(ii) if $a_{11} < 0$ and $a_{11}^2 < 4C$, then λ_2, λ_3 form a pair of complex conjugate roots with a negative real part, and $E^3_{S_1}$ is a stable focus;
(iii) if $a_{11} > 0$ and $a_{11}^2 \geq 4C$, then $\lambda_3 \geq \lambda_2 > 0$ are two (possibly coincident) positive real roots, and $E^3_{S_1}$ is an unstable node;
(iv) if $a_{11} > 0$ and $a_{11}^2 < 4C$, then λ_2, λ_3 form a pair of complex conjugate roots with a positive real part, and $E^3_{S_1}$ is an unstable focus.

When $a_{11} = 0$, since $C > 0$, the characteristic roots $\lambda_{2,3} = \pm i\sqrt{C}$ form a pair of purely imaginary roots, which suggests that a Hopf bifurcation may occur at $E^3_{S_1}$. To guarantee the occurrence of the Hopf bifurcation, the transversality condition must be verified. Taking the carrying capacity K as the bifurcation parameter, one computes

$$\frac{\partial a_{11}}{\partial K} = \frac{r x_1}{K^2}\left(2 - \frac{1}{1 + bx_1}\right) > 0,$$

which is strictly positive for any $x_1 > 0$. Therefore, as K passes through the critical value at which $a_{11} = 0$, the pair of complex eigenvalues crosses the imaginary axis transversally, and the system undergoes a Hopf bifurcation. The stability of the bifurcating periodic orbit is determined by the first Lyapunov coefficient, whose computation is beyond the scope of the present work. For the parameter sets adopted in the numerical simulations of Section 4, one verifies that $a_{11} < 0$ and $a_{11}^2 < 4C$, so that $E^3_{S_1}$ is a stable focus, which is consistent with the spiral convergence observed in the simulations.

2.3. Dynamics of subsystem S_2

This section focuses on the existence and local stability properties of the nonnegative equilibrium points of subsystem S_2. Subsystem S_2 admits three nonnegative equilibrium points, given by

$$E^1_{S_2} = (0, 0, 0), \qquad E^2_{S_2} = (K, 0, 0), \qquad E^3_{S_2} = (x_2, y_{n2}, y_{m2}),$$

and

$$y_{n2} = \frac{\mu_m y_{m2}}{\eta_2 \alpha x_2}, \quad y_{m2} = \frac{1}{\delta}\left(\frac{\eta_1 a_n x_2}{1 + bx_2} - \mu_n\right),$$

while x_2 needs to be solved via Ferrari's method (the detailed calculation procedures are provided in Appendix A.

The existence of these equilibrium points implies the following results.

- The boundary equilibria $E^1_{S_2} = (0, 0, 0)$ and $E^2_{S_2} = (K, 0, 0)$ are always present.

- The positive equilibrium $E^3_{S_2} = (x_2, y_{n2}, y_{m2})$ exists if and only if the root x_2 of the quartic equation in the Appendix satisfies $\mu_n/(\eta_1 a_n - \mu_n b) < x_2 < K$.

Based on the above results, the Jacobian matrix of subsystem S_2 is obtained as

$$\mathbf{J}|_{E^i_{S_2}(x,y_n,y_m)} = \begin{pmatrix} r\left(1 - \dfrac{2x}{K}\right) - \dfrac{a_n y_n}{(1+bx)^2} - cy_n & -\left(\dfrac{a_n}{1+bx} + c\right)x & 0 \\ \dfrac{\eta_1 a_n y_n}{(1+bx)^2} & \dfrac{\eta_1 a_n x}{1+bx} - \mu_n - \delta y_m & -\delta y_n \\ \eta_2 \alpha y_n & \eta_2 \alpha x & -\mu_m \end{pmatrix}\Bigg|_{E^i_{S_2}(x,y_n,y_m)},$$

where $i = 1, 2, 3$. Let $\lambda_j (j = 1, 2, 3)$ represent the three eigenvalues of the characteristic equation evaluated at $E^i_{S_2}$. The local stability of the equilibrium point $E^i_{S_2} = (x, y_n, y_m)$ is determined by these eigenvalues. At the equilibrium point $E^1_{S_2} = (0, 0, 0)$, the eigenvalues of the characteristic equation are $\lambda_1 = r$, $\lambda_2 = -\mu_n$, and $\lambda_3 = -\mu_m$, indicating that $E^1_{S_2} = (0, 0, 0)$ is an unstable saddle point.

The characteristic equation corresponding to $E^2_{S_2} = (K, 0, 0)$ is

$$(\lambda + r)\left(\lambda - \frac{\eta_1 a_n K}{1 + bK} + \mu_n\right)(\lambda + \mu_m) = 0,$$

where

$$\lambda_1 = -r, \quad \lambda_2 = \frac{\eta_1 a_n K}{1 + bK} - \mu_n, \quad \lambda_3 = -\mu_m.$$

Since $\lambda_1, \lambda_3 < 0$, the stability of $E^2_{S_2}$ depends on λ_2: when $\dfrac{\eta_1 a_n K}{1 + bK} < \mu_n$, the equilibrium $E^2_{S_2}$ represents a stable node. In contrast, when $\dfrac{\eta_1 a_n K}{1 + bK} > \mu_n$, $E^2_{S_2}$ becomes an unstable saddle point.

The characteristic equation related to $E^3_{S_2} = (x_2, y_{n2}, y_{m2})$ is expressed in the form below:

$$\lambda^3 + a_2\lambda^2 + a_1\lambda + a_0 = 0$$

and

$$\begin{aligned}
a_2 &= \mu_m - p,\\
a_1 &= -p\mu_m + \delta\eta_2\alpha x y_n + \eta_1 a_n q\frac{xy_n}{(1+bx)^2},\\
a_0 &= -p\delta\eta_2\alpha x y_n + \mu_m\eta_1 a_n q\frac{xy_n}{(1+bx)^2} - \delta\eta_2\alpha q x (y_n)^2,
\end{aligned}$$

where

$$p = r\left(1 - \frac{2x}{K}\right) - \frac{a_n y_n}{(1+bx)^2} - cy_n, \quad q = \frac{a_n}{1+bx} + c.$$

According to the Routh–Hurwitz criterion [17], when the conditions $a_2 > 0$, $a_1 > 0$, $a_0 > 0$ and $a_2a_1 > a_0$, hold, $E^3_{S_2}$ is identified as either a stable focus or a stable node.

2.4. Basic properties

In this section, some definitions, a theorem and symbols regarding general non-smooth Filippov systems [5, 16, 18, 19] will be introduced.

For a general Filippov system, the contact between the smooth vector fields F_{S_1} and F_{S_2} (i.e., subsystems S_1 and S_2) and the discontinuous boundary Σ is characterized by the directional Lie derivative [19]:

$$L_{\mathbf{F}_{S_i}}(H(\mathbf{X})) = \langle \nabla H(\mathbf{X}), \mathbf{F}_{S_i}(\mathbf{X})\rangle, \quad i = 1, 2,$$

where $\langle , \rangle$ indicates the standard scalar product and $\nabla H(\mathbf{X})$ denotes the gradient of $H(\mathbf{X})$, which is non-vanishing on Σ . The higher–order Lie derivatives are given by

$$L^n_{\mathbf{F}_{S_i}}(H(\mathbf{X})) = \langle \nabla L^{n-1}_{\mathbf{F}_{S_i}}(H(\mathbf{X})), \mathbf{F}_{S_i}(\mathbf{X})\rangle, \quad n = 1, 2, \ldots$$

Let

$$\sigma(\mathbf{X}) \doteq \langle \nabla H(\mathbf{X}), \mathbf{F}_{S_1}(\mathbf{X})\rangle\langle \nabla H(\mathbf{X}), \mathbf{F}_{S_2}(\mathbf{X})\rangle = L_{\mathbf{F}_{S_1}}(H(\mathbf{X}))L_{\mathbf{F}_{S_2}}(H(\mathbf{X})).$$

On Σ, we distinguish the following regions:

(i) Crossing region, defined by $\Sigma_C \doteq \{\mathbf{X} \in \Sigma \mid \sigma(\mathbf{X}) > 0\}$;

(ii) Sliding region, defined by $\Sigma_S \doteq \{\mathbf{X} \in \Sigma \mid \sigma(\mathbf{X}) < 0\}$. More precisely, Σ_S can be separated into the two following regions:

(a) Attractive sliding region, defined by

$$\Sigma_A \doteq \left\{\mathbf{X} \in \Sigma_S \mid L_{\mathbf{F}_{S_1}}(H(\mathbf{X})) > 0 \text{ and } L_{\mathbf{F}_{S_2}}(H(\mathbf{X})) < 0\right\}.$$

(b) Repulsive (or escaping) sliding region, defined by

$$\Sigma_E \doteq \left\{\mathbf{X} \in \Sigma_S \mid L_{\mathbf{F}_{S_1}}(H(\mathbf{X})) < 0 \text{ and } L_{\mathbf{F}_{S_2}}(H(\mathbf{X})) > 0\right\}.$$

Note that when $\mathbf{X} \in \Sigma_S$, by Filippov's convex method [6, 16, 20] , the sliding vector field is a convex combination of the two vector fields $\mathbf{F}_{S_1}$ and $\mathbf{F}_{S_2}$, defined as

$$\mathbf{F}_{\Sigma_S}(\mathbf{X}) = \lambda\mathbf{F}_{S_1}(\mathbf{X}) + (1-\lambda)\mathbf{F}_{S_2}(\mathbf{X}), \tag{2.2}$$

where the value of λ is chosen such that $L_{\mathbf{F}_{\Sigma_S}}(H(\mathbf{X})) = 0$, i.e.,

$$\lambda = \lambda(\mathbf{X}) = \frac{L_{\mathbf{F}_{S_2}}(H(\mathbf{X}))}{L_{\mathbf{F}_{S_2}}(H(\mathbf{X})) - L_{\mathbf{F}_{S_1}}(H(\mathbf{X}))} = \frac{\langle \nabla H(\mathbf{X}), \mathbf{F}_{S_2}(\mathbf{X}) \rangle}{\langle \nabla H(\mathbf{X}), \mathbf{F}_{S_2}(\mathbf{X}) - \mathbf{F}_{S_1}(\mathbf{X}) \rangle} \in (0, 1).$$

Additionally, the corresponding definitions of various equilibrium points of Filippov system (2.1) are as follows.

Definition 2.1. *A point $E(x, y_n, y_m)$ is called a regular equilibrium of Filippov system* (2.1) *if it is an equilibrium of the subsystem S_1 or S_2, i.e., $\mathbf{F}_{S_1}(E) = 0$ or $\mathbf{F}_{S_2}(E) = 0$. More precisely, it is an admissible equilibrium if*

$$\mathbf{F}_{S_1}(E) = 0 \quad \textit{and} \quad E(x, y_n, y_m) \in S_1,$$

or

$$\mathbf{F}_{S_2}(E) = 0 \quad \textit{and} \quad E(x, y_n, y_m) \in S_2.$$

Alternatively, $E(x, y_n, y_m)$ is called a virtual equilibrium if

$$\mathbf{F}_{S_1}(E) = 0 \quad \textit{and} \quad E(x, y_n, y_m) \in S_2,$$

or

$$\mathbf{F}_{S_2}(E) = 0 \quad \textit{and} \quad E(x, y_n, y_m) \in S_1.$$

Remark 2.1. *Note that in [21], the point $E(x, y_n, y_m)$ is also called a regular equilibrium if $\mathbf{F}_{S_1}(E) = 0$ and $E(x, y_n, y_m) \in S_1$ (or $\mathbf{F}_{S_2}(E) = 0$ and $E(x, y_n, y_m) \in S_2$).*

Definition 2.2. *A point $E = (x, y_n, y_m)$ is called a boundary equilibrium of Filippov system* (2.1) *if $\mathbf{F}_{S_1}(E) = 0$ (or $\mathbf{F}_{S_2}(E) = 0$) with $E = (x, y_n, y_m) \in \Sigma$.*

Definition 2.3. *A point $E(x, y_n, y_m)$ is called a pseudo-equilibrium of Filippov system* (2.1) *if it is an equilibrium of the sliding dynamical equation* (2.2)*, i.e., $\mathbf{F}_{\Sigma_S}(E) = 0$ and $E(x, y_n, y_m) \in \Sigma_S$. Moreover, if the point $E(x, y_n, y_m) \in \Sigma_C$ satisfies $\mathbf{F}_{\Sigma_S}(E) = 0$, we say $E(x, y_n, y_m)$ is a virtual pseudo-equilibrium [18, 22].*

Definition 2.4. *A point $E(x, y_n, y_m)$ is called a tangent point of Filippov system* (2.1) *if $H(E) = 0$ and $L_{\mathbf{F}_{S_1}}(H(E)) = 0$ (or $H(E) = 0$ and $L_{\mathbf{F}_{S_2}}(H(E)) = 0$). Moreover, the tangent point $E(x, y_n, y_m)$ is said to be visible if $L^2_{\mathbf{F}_{S_1}}(H(E)) < 0$ and invisible if $L^2_{\mathbf{F}_{S_1}}(H(E)) > 0$. Analogously, for a tangent point of F_{S_2}, it is visible if $L^2_{\mathbf{F}_{S_2}}(H(E)) > 0$ and invisible if $L^2_{\mathbf{F}_{S_2}}(H(E)) < 0$ [16, 19].*

3. Sliding dynamics of Filippov system (2.1)

This section presents the principal features of Filippov system (2.1), encompassing the sliding region, tangent points, regular equilibrium points, boundary equilibrium points, virtual equilibrium points, and the associated sliding vector field.

3.1. Existence of a sliding region

Based on the definition of the sliding region Σ_S in Section 2, the inequality $\sigma(\mathbf{X}) < 0$ can be expressed as:

$$\left(\frac{\eta_1 a_n x y_n}{1+bx} - \mu_n y_n + \beta\mu_m y_m\right)\left(\frac{\eta_1 a_n x y_n}{1+bx} - \mu_n y_n - \delta y_m y_n + \beta\mu_m y_m - \beta\eta_2\alpha x y_n\right) < 0. \tag{3.1}$$

The formation of an attractive sliding region requires the vector fields of the two subsystems to point toward the switching surface. On Σ, the condition $H(x, y_n, y_m) = 0$ gives $y_n = \beta y_m + \gamma$; substituting this into the two Lie derivatives yields

$$F_+(x, y_m) = \frac{\eta_1 a_n x(\beta y_m + \gamma)}{1+bx} - \mu_n(\beta y_m + \gamma) + \beta\mu_m y_m$$

and

$$F_-(x, y_m) = \frac{\eta_1 a_n x(\beta y_m + \gamma)}{1+bx} - \mu_n(\beta y_m + \gamma) - \delta y_m(\beta y_m + \gamma) + \beta\mu_m y_m - \beta\eta_2\alpha x(\beta y_m + \gamma),$$

so that the attractive sliding region is characterized by the two inequalities $F_+(x, y_m) > 0$ and $F_-(x, y_m) < 0$ holding simultaneously. After calculation, the two functions F_+ and F_- can be rewritten with the help of the auxiliary variables

$$\begin{aligned} A &= \frac{\eta_1 a_n x}{1+bx} - \mu_n, \qquad & B &= A + \mu_m, \\ C &= A - \beta\eta_2\alpha x, \qquad & D &= \beta B - \beta^2\eta_2\alpha x - \delta\gamma, \end{aligned}$$

namely, $F_+(x, y_m) = \gamma A + \beta B y_m$ and $F_-(x, y_m) = \gamma C + D y_m - \delta\beta y_m^2$.

(1) Setting $F_+(x, y_m) = 0$ yields

$$y_{m0} = -\frac{\gamma A}{\beta B} \quad (\text{when } B \neq 0).$$

(2) Setting $F_-(x, y_m) = 0$ and solving the quadratic equation gives

$$y_{m1} = \frac{D - \sqrt{\Delta}}{2\delta\beta}, \qquad y_{m2} = \frac{D + \sqrt{\Delta}}{2\delta\beta} \quad (y_{m1} \leq y_{m2}),$$

where

$$\Delta = D^2 + 4\delta\beta\gamma C.$$

The possible cases that may arise in the sliding domain are classified as follows:

(i) When $B > 0$:
(a) If $\Delta > 0$, $\Sigma_{A1} = (\max(y_{m0}, 0),\ y_{m1}) \cup (\max(y_{m0}, y_{m2}),\ \infty)$.
(b) If $\Delta \leq 0$, $\Sigma_{A2} = (\max(y_{m0}, 0),\ \infty)$.

(ii) When $B < 0$:
(a) If $\Delta > 0$, $\Sigma_{A3} = [0,\ \min(y_{m0}, y_{m1})) \cup (y_{m2},\ y_{m0})$.
(b) If $\Delta \leq 0$, $\Sigma_{A4} = [0,\ y_{m0})$.

(iii) When $B = 0$, $F_+(x, y_m) = \gamma A$ is a constant:
(a) If $A > 0$, then $F_+(x, y_m) > 0$ holds for all cases,
where

$$\Sigma_{A5} = \begin{cases} [0, y_{m1}) \cup (y_{m2}, +\infty), & \Delta > 0, \\ [0, +\infty), & \Delta \leq 0. \end{cases}$$

(b) If $A \leq 0$, then $\Sigma_{A6} = \emptyset$.

The existence of the sliding mode domain can be verified by determining the effective interval over which the sliding mode is defined.

3.2. Equilibrium point classification and sliding vector field dynamics

The primary objective of this section is to perform a comprehensive analysis of the four types of equilibria present in Filippov system (2.1): regular equilibrium, virtual equilibrium, boundary equilibrium, and pseudo-equilibrium [23]. These concepts were introduced in Section 2. The three equilibria of subsystems S_1 and S_2 are given by:

$$E^1_{S_i} = (0, 0, 0), \qquad E^2_{S_i} = (K, 0, 0), \qquad (i = 1, 2).$$

In this case, $E^1_{S_1}$ and $E^2_{S_1}$ are always regular equilibria of subsystem S_1, while $E^1_{S_2}$ and $E^2_{S_2}$ are always virtual equilibria of subsystem S_2 (they lie in S_1). Next, we analyze whether the equilibria $E^3_{S_1}$ and $E^3_{S_2}$ are virtual or regular.

For $E^3_{S_1}$, since $y_m = 0$, one has $H(E^3_{S_1}) = y_{n1} - \gamma$: if $y_{n1} < \gamma$, then $E^3_{S_1} \in S_1$ and it represents a regular equilibrium; if $y_{n1} > \gamma$, then $E^3_{S_1} \in S_2$ and it represents a virtual equilibrium; if $y_{n1} = \gamma$, then $E^3_{S_1} \in \Sigma$ and it represents a boundary equilibrium. For $E^3_{S_2}$, one has $H(E^3_{S_2}) = y_{n2} - \beta y_{m2} - \gamma$: if $H(E^3_{S_2}) < 0$, then $E^3_{S_2} \in S_1$ and it represents a virtual equilibrium; if $H(E^3_{S_2}) > 0$, then $E^3_{S_2} \in S_2$ and it represents a regular equilibrium; if $H(E^3_{S_2}) = 0$, then $E^3_{S_2} \in \Sigma$ and it represents a boundary equilibrium.

The pseudo-equilibrium points of the Filippov system (2.1) correspond to the equilibrium points of the sliding vector field (2.2). Therefore, the first step is to identify the equilibrium points of this sliding vector field (2.2). Using Filippov convex method [6, 16, 20], the differential equation governing the sliding dynamics within the sliding region Σ_A can be expressed as:

$$\begin{cases} \dfrac{dx}{dt} = rx\left(1 - \frac{x}{K}\right) - \frac{a_n x(\beta y_m + \gamma)}{1 + bx} - cx(\beta y_m + \gamma)\frac{M}{N}, \\ \dfrac{dy_m}{dt} = -\mu_m y_m + \eta_2 \alpha x(\beta y_m + \gamma)\frac{M}{N}, \end{cases} \tag{3.2}$$

where

$$M = \frac{\eta_1 a_n x}{1 + bx} - \mu_n + \frac{\beta \mu_m y_m}{\beta y_m + \gamma}, \qquad N = \delta y_m + \beta \eta_2 \alpha x.$$

Pseudo-equilibria are determined by the equilibrium conditions of the sliding-mode dynamical equations on the surface $H = 0$, and the system of algebraic equations (3.2) they satisfy takes an implicit form. After elimination, a high-order polynomial equation with respect to x (degree ≥ 5) is obtained. According to Galois theory, such equations admit no general radical solutions

and cannot be further simplified into explicit analytical expressions. Therefore, we adopt numerical methods (e.g., the Newton–Raphson method) to solve the system within the biologically feasible region $0 < x < K$, $y_m > 0$. All numerical solutions are verified using the sliding-mode reachability condition $\lambda \in [0, 1]$, which is equivalent to $1 - \lambda = M/N \in [0, 1]$, to guarantee practical physical significance.

4. Numerical simulation

By means of analytical deduction, the preceding sections conducted theoretical research focusing on the existence of equilibrium points, sliding modes, and tangency points, alongside the dynamic features belonging to the sliding vector field of the studied system. A large set of numerical simulations based on MATLAB was therefore conducted, aiming to validate the above theoretical results and delve into more sophisticated dynamical phenomena.

4.1. Long-transient orbital behaviors under monostable and bistable regimes

In Figures 1–4, panel (a) shows the three-dimensional state-space trajectory plot in (x, y_n, y_m) space, panel (b) is the time-series plot, and panel (c) denotes the phase projection plot in (x, y_n) space. For Figure 1, the parameter a_n is set to 0.7. Under this set of parameters, the system exhibits a single attracting state within the tested initial-condition domain and thus operates in the monostable regime [24]. Trajectories spiral for a long time near the Filippov switching manifold and sliding region, and the time-series exhibit damped oscillations lasting for more than one thousand time units. Although all sampled trajectories converge to the same attracting state, they converge extremely slowly and exhibit nearly persistent oscillations within a finite observation window. It should be noted that, under this parameter set, the positive equilibria $E^3_{S_1}$ and $E^3_{S_2}$ of the two subsystems are both virtual equilibria ($y_{n1} - \gamma > 0$ and $y_{n2} - \beta y_{m2} - \gamma < 0$); hence the attracting state observed in the simulation is not a subsystem equilibrium itself but an attracting state of the full piecewise-smooth system associated with the switching manifold Σ. For Figure 2, the parameter is adjusted to $a_n = 0.8$ on the basis of Figure 1; for Figure 3, $\mu_n = 0.2$ is adopted; for Figure 4, $a_n = 0.9$, $\mu_n = 0.2$, $r = 2.6$, and $\gamma = 2$ are set. In Figures 2–4, the system exhibits two coexisting attracting states within the tested initial-condition domain and hence bistable behavior [25]. Three sets of different initial conditions are selected for numerical integration. Trajectories corresponding to distinct initial conditions also undergo long-time spiral oscillations near the switching manifold and eventually converge to two different attracting states, respectively. Under these parameter sets, the positive equilibria of the two subsystems are again virtual, so the two attracting states observed in the simulations are associated with the switching manifold Σ rather than with the subsystem equilibria themselves. Comparing the phenomena under monostable and bistable regimes, it can be seen that long-transient damped oscillations are not unique to bistability; they can also occur within monostable parameter regions. It should be noted that both monostable and bistable cases in this section correspond to genuine attractor configurations of the system, while trajectories exhibit slowly converging transient oscillations. This raises a key question: Do long-lasting oscillations observed in numerical simulations represent real steady-state oscillatory attractors, or merely transient dynamics during the convergence process?

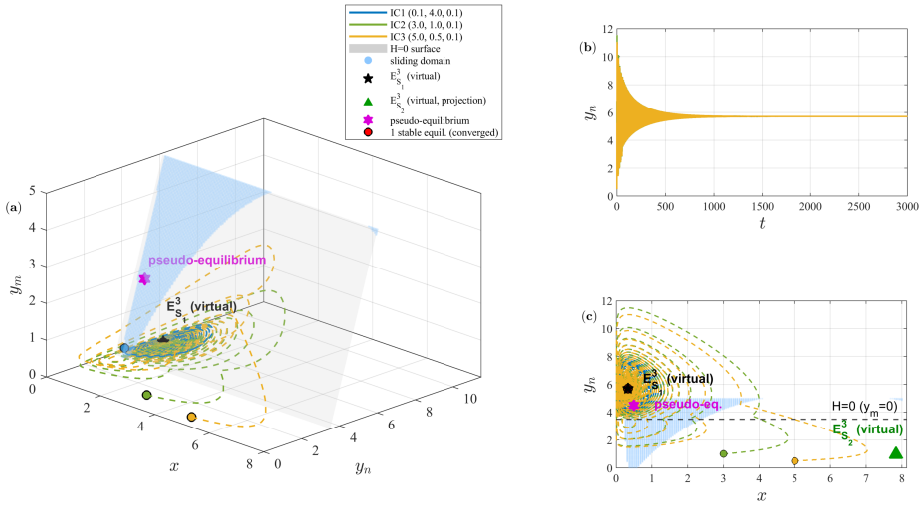


Figure 1. (*a*) three-dimensional state-space trajectory plot in (x, y_n, y_m) space; (*b*) time Series plot; (*c*) phase projection plot in (x, y_n) space. Parameters of system (2.1): $K = 10$, $a_n = 0.7$, $b = 0.1$, $c = 0.5$, $\mu_n = 0.18$, $\mu_m = 0.18$, $\eta_1 = 0.8$, $\eta_2 = 0.9$, $\alpha = 0.5$, $\delta = 0.12$, $r = 4$, $\gamma = 3.5$, $\beta = 0.5$.

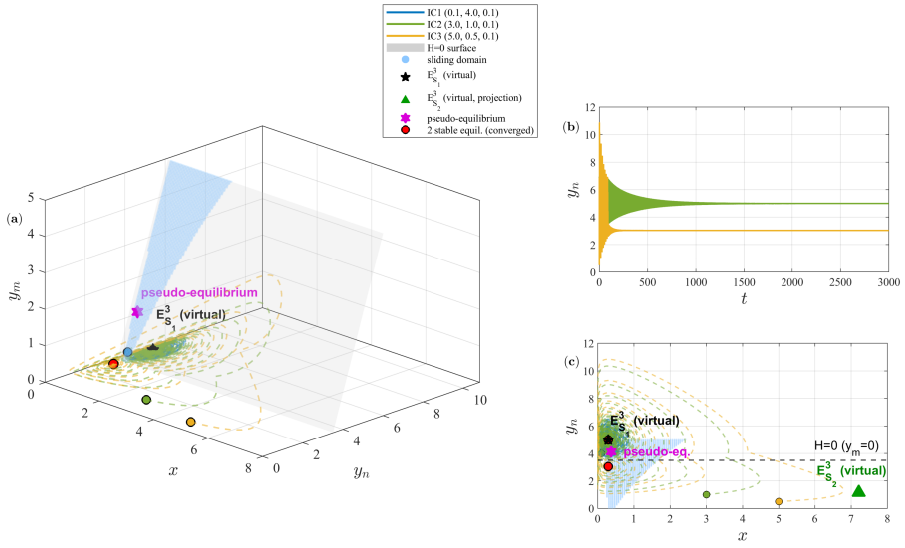


Figure 2. (*a*) three-dimensional state-space trajectory plot in (x, y_n, y_m) space; (*b*) time Series plot; (*c*) phase projection plot in (x, y_n) space. Parameters of system (2.1): $K = 10$, $a_n = 0.8$, $b = 0.1$, $c = 0.5$, $\mu_n = 0.18$, $\mu_m = 0.18$, $\eta_1 = 0.8$, $\eta_2 = 0.9$, $\alpha = 0.5$, $\delta = 0.12$, $r = 4$, $\gamma = 3.5$, $\beta = 0.5$.

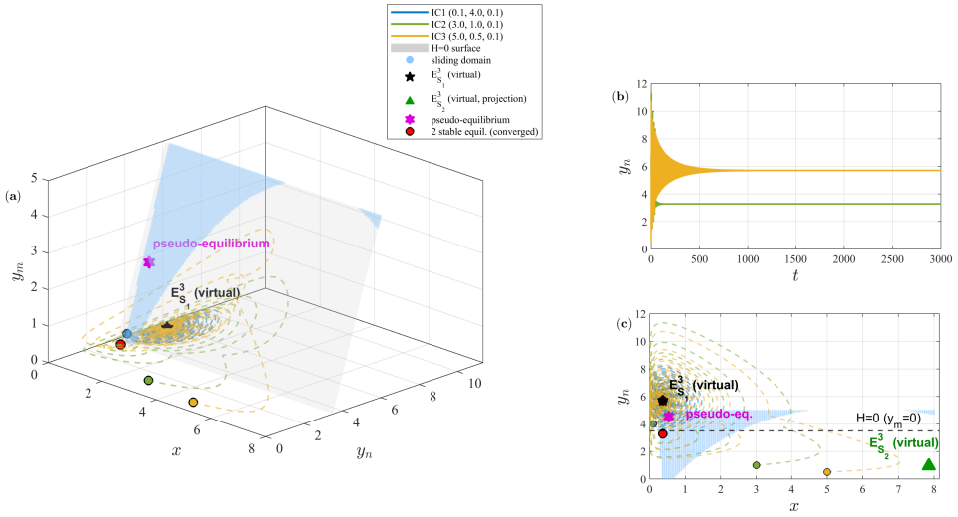


Figure 3. (*a*) three-dimensional state-space trajectory plot in (x, y_n, y_m) space; (*b*) time Series plot; (*c*) phase projection plot in (x, y_n) space. Parameters of system (2.1): $K = 10$, $a_n = 0.7$, $b = 0.1$, $c = 0.5$, $\mu_n = 0.20$, $\mu_m = 0.18$, $\eta_1 = 0.8$, $\eta_2 = 0.9$, $\alpha = 0.5$, $\delta = 0.12$, $r = 4$, $\gamma = 3.5$, $\beta = 0.5$.

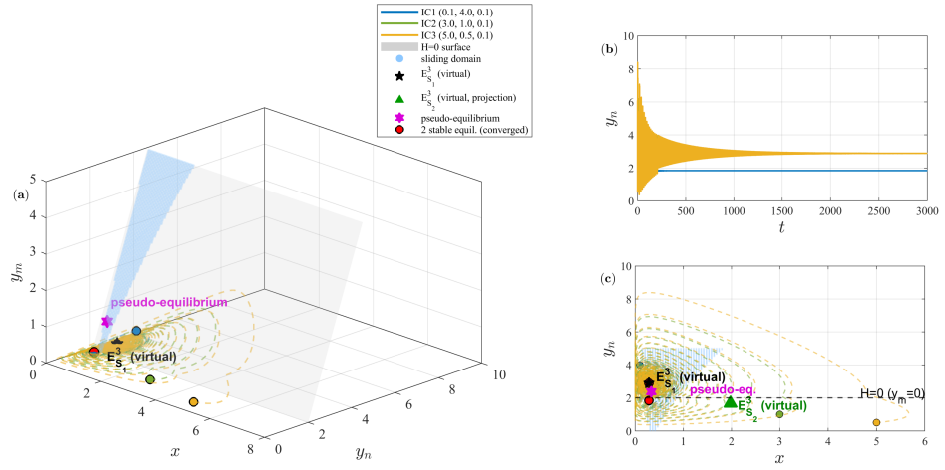


Figure 4. (*a*) three-dimensional state-space trajectory plot in (x, y_n, y_m) space; (*b*) time Series plot; (*c*) phase projection plot in (x, y_n) space. Parameters of system (2.1): $K = 10$, $a_n = 0.9$, $b = 0.1$, $c = 0.5$, $\mu_n = 0.20$, $\mu_m = 0.18$, $\eta_1 = 0.8$, $\eta_2 = 0.9$, $\alpha = 0.5$, $\delta = 0.12$, $r = 2.6$, $\gamma = 2$, $\beta = 0.5$.

4.2. Apparent spurious limit cycles generated by short-time simulations

Under both monostable and bistable parameter conditions, trajectories exhibit prominent apparent oscillatory features if only the early-stage simulation results of finite duration are examined.

For the monostable case shown in Figure 5, we set the parameters following the configuration in Figure 1. Within a short integration time, trajectories spiral repeatedly around the equilibrium point on the phase plane and become nearly closed. The corresponding time-series displays sustained oscillations with very slight amplitude variation. Based solely on this limited segment of data, such dynamical can easily behaviors misidentified as a stable limit cycle. Nevertheless, when the simulation time is substantially extended, the oscillation amplitude decays gradually and trajectories eventually converge to the same stable attracting state. This demonstrates that the observed oscillation is merely a transient behavior during convergence. For the bistable case shown in Figure 6, we set two parameters following the configuration in Figure 2. Trajectories starting from different initial conditions also exhibit long-time spiral motion near the switching manifold. Within a short-time window, the two sets of trajectories each form approximately closed curves, and the time-series show sustained oscillations, which are readily misinterpreted as two distinct steady-state limit cycles of the system. Provided that the integration time is sufficiently long, the oscillation amplitudes of both trajectories decrease progressively, and they converge respectively to the two genuine stable attracting states of the system. The above-mentioned artifacts stem entirely from finite simulation duration and do not alter the intrinsic monostable or bistable properties of the system within the parameter domains examined. The number and type of the attracting states involved are fixed for each parameter set tested. It is the convergence process of long transients that conceals the final steady state. Relying merely on short-time numerical simulations, one can hardly distinguish genuine steady-state limit cycles from apparent oscillations induced by long-transient dynamics. More precisely, these are apparent spurious limit cycles generated by short-time simulations [26–28].

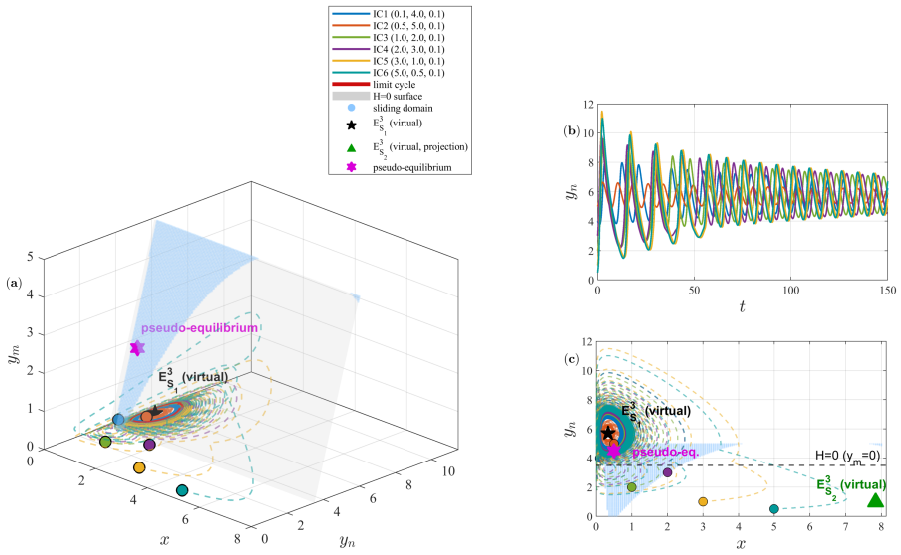


Figure 5. (*a*) three-dimensional state-space trajectory plot in (x, y_n, y_m) space; (*b*) time Series plot; (*c*) phase projection plot in (x, y_n) space. Parameters of system (2.1): $K = 10$, $a_n = 0.7$, $b = 0.1$, $c = 0.5$, $\mu_n = 0.18$, $\mu_m = 0.18$, $\eta_1 = 0.8$, $\eta_2 = 0.9$, $\alpha = 0.5$, $\delta = 0.12$, $r = 4$, $\gamma = 3.5$, $\beta = 0.5$. Simulation time $T = 150$.

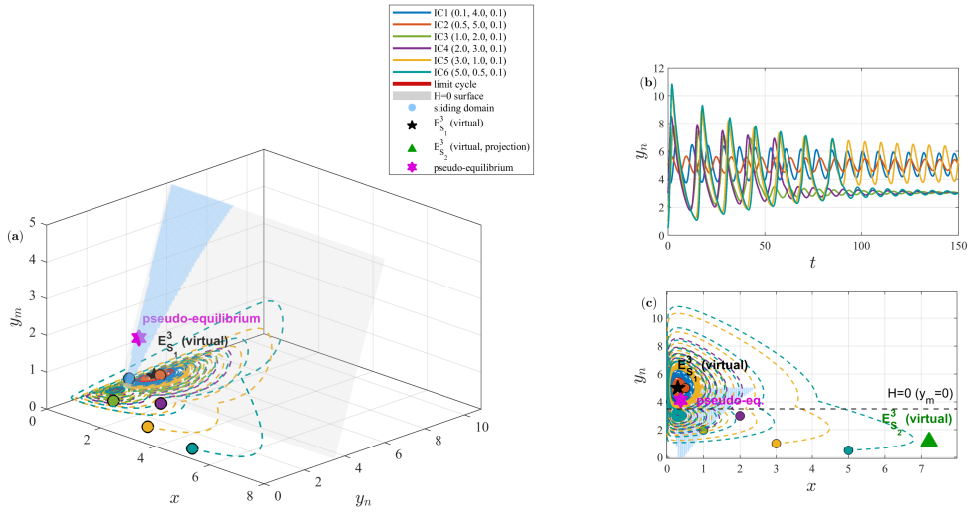


Figure 6. (*a*) three-dimensional state-space trajectory plot in (x, y_n, y_m) space; (*b*) time Series plot; (*c*) phase projection plot in (x, y_n) space. Parameters of system (2.1): $K = 10$, $a_n = 0.8$, $b = 0.1$, $c = 0.5$, $\mu_n = 0.18$, $\mu_m = 0.18$, $\eta_1 = 0.8$, $\eta_2 = 0.9$, $\alpha = 0.5$, $\delta = 0.12$, $r = 4$, $\gamma = 3.5$, $\beta = 0.5$. Simulation time $T = 150$.

4.3. Quantitative identification and result analysis of long transients

It can be seen from the above monostable and bistable parameter regimes that the Filippov system can generate transient oscillations with extremely slow convergence rates. Phase trajectories and time-domain time-series can only provide qualitative results, and cannot rigorously distinguish whether the observed oscillations correspond to steady-state limit cycles, chaotic motions, or slowly-decaying transient responses. When the simulation time is short, transient oscillations may exhibit characteristics nearly identical to those of steady-state oscillations, which readily lead to misjudgment of dynamical behaviors.

To distinguish steady-state attractors from transient behaviors, we compute the maximum Lyapunov exponents over the parameter plane and obtain the global dynamical landscape of the system (Figure 7). For a trajectory $X(t)$ of system (2.1) and an infinitesimal perturbation $\delta X(t)$ evolving along the tangent linearization, the maximum Lyapunov exponent is defined as

$$\lambda_{\max} = \lim_{t\to\infty} \frac{1}{t} \ln \frac{\|\delta X(t)\|}{\|\delta X(0)\|}.$$

Numerically, $\lambda_{\max}$ is computed by a variational (Benettin-type) scheme [29]: the tangent vector δX is integrated together with the reference trajectory by the fixed-step fourth-order Runge–Kutta method (step size $h = 0.02$), using the Jacobian matrix of the active smooth branch of the Filippov system and the convex-combination sliding field within the sliding region; the tangent vector is renormalized at unit-time intervals; a transient of 200 time units is discarded; and the exponent is averaged over a subsequent window of 200 time units. The computation is repeated over a uniform 200×200 grid

on the parameter plane $(\beta, \gamma) \in [0.2, 0.4] \times [1, 4]$ with the remaining parameters fixed, to produce the landscape shown in Figure 7. The red-orange regions correspond to positive maximum Lyapunov exponents, indicating genuine chaos; the blue regions denote negative Lyapunov exponents. The parameters focused on in this work lie within a narrow yellow-green transitional layer where the largest Lyapunov exponent (LLE) approaches zero from below and remains negative. This directly rules out the possibility of chaotic attractors. The parameter plane exhibits clear dynamical partitioning: the system behaves chaotically in the lower region of the parameter plane. Above the chaotic zone, the narrow parameter interval with LLE ≈ 0 is where long transients predominantly emerge, and this phenomenon is highly sensitive to parameter variations. With further upward adjustment of the vertical parameter, the system enters a strongly stable regime, and transient processes are markedly shortened. The scattered short yellow-green streaks visible in the plot are numerical artifacts originating from the discontinuous switching of the Filippov system.

Lyapunov-exponent analysis [11] has ruled out chaos; nevertheless, it remains necessary to verify that this slow convergence is not a spurious artifact caused by numerical integration. The semi-logarithmic decay curve of oscillation amplitude is plotted in Figure 8. For an exponential-decay process, the amplitude decreases approximately along a straight line in the semi-logarithmic coordinate system [12]. For simulations carried out with core parameters, the obtained relaxation-time constants for two of the three parameter sets are in high agreement with the theoretical values computed via linearization of the Jacobian matrix at the corresponding subsystem equilibrium points. We remark that for these two parameter sets in Figure 8, the corresponding subsystem equilibrium is virtual and the observed attracting state lies on the switching manifold Σ; the measured decay rates ($\tau \approx 1280$ and $\tau \approx 435$) are in close agreement with the eigenvalue estimates obtained by linearizing at the corresponding subsystem equilibria ($\tau \approx 1277$ and $\tau \approx 435$), which indicates that the slow spiral contraction of the trajectories is organized by these virtual equilibria. For the remaining parameter set, the corresponding subsystem equilibrium is regular, and the measured effective decay ($\tau \approx 155$) is faster than the smooth linearization estimate ($\tau \approx 485$); this difference is consistent with the additional dissipation induced by the repeated crossings of the switching surface during the approach. This demonstrates that slow decay represents an intrinsic dynamical behavior of the system, and spurious effects originating from numerical computation can be excluded. Multiple comparative results show that tiny parameter variations can substantially alter the duration of transient behavior. For three sets of distinct parameters, the oscillation amplitudes all decrease approximately linearly in the semi-logarithmic coordinate system, consistent with exponential-decay characteristics, which further confirms that the oscillations are transient behaviors converging toward the equilibrium point. Nevertheless, the decay time constants τ differ considerably across parameters. For some parameter sets, the decay constant is on the order of hundreds, and trajectories converge relatively rapidly. For another parameter set, the time constant reaches 1280; thousands of time units are required for the amplitude to drop below the detection threshold. A large time constant implies an extremely long convergence process. Even though the system eventually converges to an equilibrium point, it still exhibits the apparent effect of sustained oscillations within a finite simulation window. The vertical dotted lines in the figure mark commonly used stopping instants for simulations. If the computation is terminated at such an instant (e.g., the $T = 150$ horizon adopted in Figures 5 and 6) while the oscillation amplitude still lies above the observation threshold, long transients are apt to be misidentified as steady-state self-sustained oscillations [10].

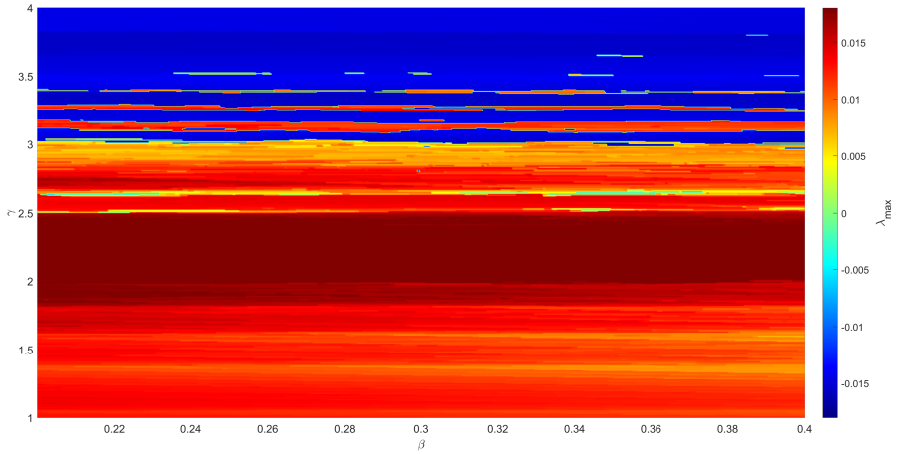


Figure 7. two-dimensional parameter scan of the maximum Lyapunov exponent over the plane $(\beta, \gamma) \in [0.2, 0.4] \times [1, 4]$ (a uniform 200×200 grid). Parameters of system (2.1): $K = 10$, $a_n = 0.95$, $b = 0.1$, $c = 0.5$, $\mu_n = 0.18$, $\mu_m = 0.18$, $\eta_1 = 0.8$, $\eta_2 = 0.9$, $\alpha = 0.5$, $\delta = 0.12$, $r = 4$.

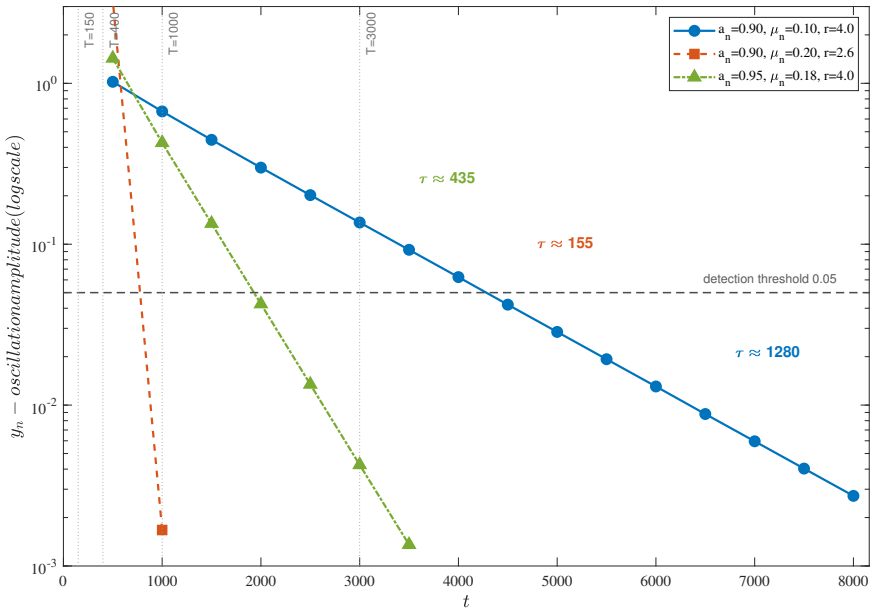


Figure 8. Semi-logarithmic decay curve of oscillation amplitude. The vertical dotted lines mark the stopping instants $T = 150$, 400, 1000, and 3000. Parameters of system (2.1): $\tau = 1280$: $K = 10$, $a_n = 0.9$, $b = 0.1$, $c = 0.5$, $\mu_n = 0.1$, $\mu_m = 0.18$, $\eta_1 = 0.8$, $\eta_2 = 0.9$, $\alpha = 0.5$, $\delta = 0.12$, $r = 4$, $\gamma = 3.5$, $\beta = 0.5$; $\tau = 155$: $K = 10$, $a_n = 0.9$, $b = 0.1$, $c = 0.5$, $\mu_n = 0.2$, $\mu_m = 0.18$, $\eta_1 = 0.8$, $\eta_2 = 0.9$, $\alpha = 0.5$, $\delta = 0.12$, $r = 2.6$, $\gamma = 3.5$, $\beta = 0.5$; $\tau = 435$: $K = 10$, $a_n = 0.95$, $b = 0.1$, $c = 0.5$, $\mu_n = 0.18$, $\mu_m = 0.18$, $\eta_1 = 0.8$, $\eta_2 = 0.9$, $\alpha = 0.5$, $\delta = 0.12$, $r = 4$, $\gamma = 3$, $\beta = 0.3$.

Such long-transient behaviors are jointly induced by two factors. First, the real parts of the eigenvalues of the Jacobian matrix at the equilibrium point are close to zero, rendering the equilibrium weakly stable. Second, geometric constraints introduced by the Filippov switching manifold and sliding region allow trajectories to spiral around the equilibrium for a long time, which further prolongs the convergence process. Combining the LLE calculations, initial-condition scanning, and amplitude-decay results, we can draw the following conclusion: within the tested parameter and initial-condition domains, the long-lasting oscillations observed under both monostable and bistable parameter regimes are neither chaotic motions nor steady-state limit cycles; they essentially belong to long-transient dynamics. For every parameter set and initial condition tested in this study, the steady state of the system is an equilibrium point of Filippov system (2.1) (a regular equilibrium or a pseudo-equilibrium on the switching manifold). The seemingly persistent oscillations merely arise from an extremely slow exponential-convergence process.

5. Conclusions

This paper investigates a Filippov piecewise-smooth dynamical system that describes the interspecific interactions among aphids, ladybugs, and ants. Aiming at the long-time oscillation phenomenon observed in numerical simulations, qualitative dynamical analysis is carried out based on phase trajectories and time series. Furthermore, quantitative computations including parameter scanning of the maximum Lyapunov exponent, multi-set initial-condition simulation verification, and semi-logarithmic amplitude-decay analysis are performed to reveal the dynamical nature and intrinsic generation mechanism of long-lasting oscillations. Under different parameters, this piecewise-smooth system can exhibit either monostable or bistable behaviors. Both steady-state configurations can trigger damped transient oscillations with extremely long duration. Multiple long-time initial-condition scans confirm that the bistability is an intrinsic dynamical property of the model. Different initial-population states converge to distinct equilibrium points, rather than representing spurious coexistence induced by transient evolution. Under short-time simulation conditions, slowly damped transient oscillations bear a high superficial resemblance to self-sustained limit cycles, which may readily lead to misinterpretation of dynamical behaviors.

Global analysis of the maximum Lyapunov exponent over the parameter plane shows that the parameter interval of interest in this work lies entirely within the non-chaotic region, which rules out chaotic attractors as the source of long-time oscillations. Long transients predominantly occur within a narrow parameter band where the maximum Lyapunov exponent approaches zero, and the dynamical behaviors are highly sensitive to parameter perturbations. The layered bifurcation structure exhibited by this autonomous unforced piecewise-smooth system differs from the Arnold-tongue resonance phenomenon in forced systems. Discrete anomalous points in the parameter diagram originate from numerical artifacts caused by the piecewise discontinuous structure.

Semi-logarithmic amplitude-decay results demonstrate that the observed oscillations strictly follow the exponential-decay law. The simulated relaxation-time constants for two of the three parameter sets agree well with the theoretical values obtained from linearization at the corresponding subsystem equilibrium points, while for the remaining set, the effective decay is faster, consistent with the switching-induced dissipation during the approach; overall, this confirms that the ultra-slow convergence is an intrinsic dynamical behavior of the system and eliminates interference from

numerical computational errors. Slight parameter variations can markedly modify the transient convergence duration. If conventional simulation truncation time is adopted before the evolution process is completed, long transients can readily be misclassified as steady-state self-sustained oscillations. Mechanism analysis reveals that long-transient behaviors arise from the coupling of two-fold effects: the weak-stability effect induced by near-zero real parts of equilibrium eigenvalues, together with geometric constraints imposed by the Filippov switching manifold and sliding region. Trajectories spiral persistently in the neighborhood of equilibria, which greatly delays the convergence of populations toward steady states. In summary, for all parameter sets and initial conditions examined in this study, the genuine steady state of this ecological piecewise-smooth system is an equilibrium point of the Filippov system (a regular equilibrium or a pseudo-equilibrium on the switching manifold). The persistent oscillations observed correspond to long-transient dynamical responses triggered when parameters are close to critical conditions. We emphasize that in the present model, the switching between the reproduction and defence strategies is governed by the hard threshold H, rather than by an adaptive optimization process of individual aphids. Accordingly, the apparent trade-off between reproduction and defensive cost should be understood as a population-level consequence of the threshold switching rule: it is the piecewise switching structure itself, rather than an optimization mechanism, that gives rise to the long-transient dynamics described above. Furthermore, the observability of long transients in real populations deserves attention. In natural ecosystems, environmental stochasticity continuously perturbs population densities; such perturbations may mask the slowly decaying oscillations or may repeatedly re-excite them near the weakly stable attracting state, so that the effective duration of the transient is substantially modified. Consequently, finite-length field time series are exposed to the same misjudgment risk identified in this study, which reinforces the practical relevance of distinguishing transient oscillations from genuine steady-state behavior in threshold-regulated ecosystems [9].

This study clarifies the identification boundary between transient oscillations and genuine steady-state behaviors in piecewise-smooth systems. It provides theoretical references for simulation analyzes of ecological models with strategy switching such as the aphid–ant–ladybug system, as well as for numerical interpretation of other discontinuous dynamical systems.

Author contributions

Zheqi Tao: Conceptualization, methodology, investigation, validation, software, formal analysis, writing original draft, writing review and editing; Yi Yang: Conceptualization, methodology, investigation, software, formal analysis, writing original draft, supervision; Changcheng Xiang: Conceptualization, methodology, software, writing original draft. All authors have read and agreed to the published version of the manuscript.

Use of Generative-AI tools declaration

The authors declare that they have not used Artificial Intelligence (AI) tools in the creation of this article.

Acknowledgments

This work was supported by the Science and Technology Research Program of Chongqing Municipal Education Commission (Grant No. KJZD-K202601201), Chongqing Natural Science Foundation (Grant No. CSTB2024NSCQ-LZX0119), the National Natural Science Foundation of China (Grant No. 12361100), the Natural Science Foundation of Chongqing (Grant No. CSTB2023NSCQ-LZX0135), and the National Foreign Expert Program (Grant No. S20250332).

Conflict of interest

The authors state that they do not have any conflicts of interest.

References

1. E. Diehl-Fleig, E. Diehl, Interactions among attending ants, brown-citrus aphids, and ladybugs in plants of Citrus sinensis, *Neotrop. Biol. Conserv.*, **13** (2018), 161–170. http://dx.doi.org/10.4013/nbc.2018.132.08
2. Y. Lv, H. Wang, J. Ding, Q. Zhu, Dynamic analysis of a stochastic three species predator-prey model with intraguild predation and predator-switching, *Commun. Nonlinear Sci.*, **157** (2026), 109748. http://dx.doi.org/10.1016/j.cnsns.2026.109748
3. Y. Wang, Z. Shen, L. Gao, X. Ma, Global analysis of a wheat aphid-ladybug model with age structure, *J. Biomath.*, **22** (2007), 59–66.
4. B. Stadler, A. F. G. Dixon, Ecology and evolution of aphid-ant interactions, *Annu. Rev. Ecol. Evol. Syst.*, **36** (2005), 345–372. http://dx.doi.org/10.1146/annurev.ecolsys.36.091704.175531
5. M. D. Bernardo, C. J. Budd, A. R. Champneys, P. Kowalczyk, *Piecewise-smooth dynamical systems: Theory and applications*, London: Springer, 2008. https://doi.org/10.1007/978-1-84628-708-4
6. A. F. Filippov, *Differential equations with discontinuous righthand sides*, Dordrecht: Springer, 1988. https://doi.org/10.1007/978-94-015-7793-9
7. Z. Zhang, R. Yang, Dynamical analysis of a reaction–diffusion Filippov food chain model with threshold control, *Phys. D*, **496** (2026), 135325. http://dx.doi.org/10.1016/j.physd.2026.135325
8. H. Zhou, S. Tang, Complex dynamics and sliding bifurcations of the Filippov Lorenz–Chen system, *Int. J. Bifurcation Chaos*, **32** (2022), 2250182. http://dx.doi.org/10.1142/S0218127422501826
9. A. Hastings, Transient dynamics and persistence of ecological systems, *Ecol. Lett.*, **4** (2001), 215–220. http://dx.doi.org/10.1046/j.1461-0248.2001.00220.x
10. D. Rockwell, E. Naudascher, Self-sustained oscillations of impinging free shear layers, *Annu. Rev. Fluid Mech.*, **11** (1979), 67–94. http://dx.doi.org/10.1146/annurev.fl.11.010179.000435
11. V. D. Pechuk, T. S. Krasnopolskaya, E. D. Pechuk, Maximum Lyapunov exponent calculation, In: *14th Chaotic modeling and simulation international conference*, 2022, 327–335. http://dx.doi.org/10.1007/978-3-030-96964-6_22

12. J. H. Dirks, V. Dürr, Biomechanics of the stick insect antenna: Damping properties and structural correlates of the cuticle, *J. Mech. Behav. Biomed. Mater.*, **4** (2011), 2031–2042. http://dx.doi.org/10.1016/j.jmbbm.2011.07.002

13. M. Forti, B. Garay, M. Koller, L. Pancioni, An experimental study on long transient oscillations in cooperative CNN rings, In: *IEEE International workshop on cellular nanoscale networks and their applications (CNNA)*, 2012. http://dx.doi.org/10.1109/CNNA.2012.6331410

14. A. Rougirel, Convergence to steady state and attractors for doubly nonlinear equations, *J. Math. Anal. Appl.*, **339** (2008), 281–294. http://dx.doi.org/10.1016/j.jmaa.2007.06.028

15. S. Tang, J. Liang, Y. Xiao, R. A. Cheke, Sliding bifurcations of Filippov two stage pest control models with economic thresholds, *SIAM J. Appl. Math.*, **72** (2012), 1061–1080. http://dx.doi.org/10.1137/110847020

16. Y. Kuznetsov, S. Rinaldi, A. Gragnani, One-Parameter bifurcations in planar Filippov systems, *Int. J. Bifurcation Chaos*, **13** (2003), 2157–2188. http://dx.doi.org/10.1142/S0218127403007874

17. E. Dejesus, C. Kaufman, Routh-Hurwitz criterion in the examination of eigenvalues of a system of nonlinear ordinary differential equations, *Phys. Rev. A*, **35** (1987), 5288–5290. http://dx.doi.org/10.1103/PhysRevA.35.5288

18. R. Cristiano, D. J. Pagano, Two-parameter boundary equilibrium bifurcations in 3D-Filippov systems, *J. Nonlinear Sci.*, **29** (2019), 2845–2875. http://dx.doi.org/10.1007/s00332-019-09560-5

19. R. Cristiano, T. Carvalho, D. J. Tonon, D. J. Pagano, Hopf and Homoclinic bifurcations on the sliding vector field of switching systems in $\mathbb{R}^3$: A case study in power electronics, *Phys. D*, **347** (2017), 12–20. http://dx.doi.org/10.1016/j.physd.2017.02.005

20. M. E. Broucke, C. C. Pugh, S. N. Simić, Structural stability of piecewise smooth systems, *Comput. Appl. Math.*, **20** (2001), 51–89.

21. W. Qin, X. Tan, M. Tosato, X. Liu, Threshold control strategy for a non-smooth Filippov ecosystem with group defense, *Appl. Math. Comput.*, **362** (2019), 124532. http://dx.doi.org/10.1016/j.amc.2019.06.046

22. M. D. Bernardo, D. J. Pagano, E. Ponce, Nonhyperbolic boundary equilibrium bifurcations in planar Filippov systems: A case study approach, *Int. J. Bifurcation Chaos*, **18** (2008), 1377–1392. http://dx.doi.org/10.1142/S0218127408021051

23. A. L. Wang, Y. N. Xiao, R. Smith, Multiple equilibria in a non-smooth epidemic model with medical-resource constraints, *Bull. Math. Biol.*, **81** (2019), 963–994. http://dx.doi.org/10.1007/s11538-018-00544-2

24. R. Sevilla-Escoboza, A. N. Pisarchik, R. Jaimes-Reátegui, G. Huerta-Cuellar, Selective monostability in multi-stable systems, *Proc. R. Soc. A*, **471** (2015), 20150005. http://dx.doi.org/10.1098/rspa.2015.0005

25. T. Guner, O. S. Bursi, A. Marzani, A. Palermo , Numerical and experimental studies on a bistable oscillator coupled with a resonator for vibration attenuation and chaos prediction, *Nonlinear Dyn.*, **114** (2026), 218. http://dx.doi.org/10.1007/s11071-025-12088-x

26. D. X. Cao, X. X. Zhou, X. Y. Guo, N. Song, Limit cycle oscillation and dynamical scenarios in piecewise-smooth nonlinear systems with two-sided constraints, *Nonlinear Dyn.*, **112** (2024), 9887–9914. http://dx.doi.org/10.1007/s11071-024-09589-6

27. M. L. V. Quyen, J. Martinerie, C. Adam, F. J. Varela, Unstable periodic orbits in human epileptic activity, *Phys. Rev. E*, **56** (1997), 3401–3411. http://dx.doi.org/10.1103/PhysRevE.56.3401

28. C. L. Pettit, P. S. Beran, Wiener-Haar expansion of airfoil limit cycle oscillations, In: *46th AIAA/ASME/ASCE/AHS/ASC structures, structural dynamics and materials conference*, 2005. http://dx.doi.org/10.2514/6.2005-1985

29. G. Benettin, L. Galgani, A. Giorgilli, J. M. Strelcyn, Lyapunov characteristic exponents for smooth dynamical systems and for Hamiltonian systems; a method for computing all of them. Part 1: Theory, *Meccanica*, **15** (1980), 9–20. http://dx.doi.org/10.1007/BF02128236

A. Appendix: Calculation of the equilibrium value x

The analytical solutions for the quartic equation of x at the positive equilibrium point of the second subsystem are presented in full below. For brevity, we first recall that the model parameters $r, K, b, c, \mu_n, \mu_m, \delta, \eta_1, \eta_2, \alpha, a_n$ are all positive constants.

$$P = \frac{\mu_m}{\eta_2 \alpha \delta}, \quad S = c.$$

The quartic equation is:

$$\tilde{a}x^4 + \tilde{b}x^3 + \tilde{c}x^2 + \tilde{d}x + \tilde{e} = 0,$$

where

$$\begin{aligned}
\tilde{a} &= rb^2, \\
\tilde{b} &= 2rb - Krb^2, \\
\tilde{c} &= -2Krb + r + KPSb(\eta_1 a_n - \mu_n b), \\
\tilde{d} &= -Kr + KP(\eta_1 a_n(a_n + S) - \mu_n b(a_n + 2S)), \\
\tilde{e} &= -KP\mu_n(a_n + S).
\end{aligned}$$

Let $x = y - \dfrac{\tilde{b}}{4\tilde{a}}$, and then the equation can be transformed into the form without a cubic term:

$$y^4 + py^2 + qy + r_0 = 0,$$

where

$$\begin{aligned}
p &= \frac{\tilde{c}}{\tilde{a}} - \frac{3\tilde{b}^2}{8\tilde{a}^2}, \\
q &= \frac{\tilde{d}}{\tilde{a}} - \frac{\tilde{b}\tilde{c}}{2\tilde{a}^2} + \frac{\tilde{b}^3}{8\tilde{a}^3}, \\
r_0 &= \frac{\tilde{e}}{\tilde{a}} - \frac{\tilde{b}\tilde{d}}{4\tilde{a}^2} + \frac{\tilde{b}^2\tilde{c}}{16\tilde{a}^3} - \frac{3\tilde{b}^4}{256\tilde{a}^4}.
\end{aligned}$$

We introduce an auxiliary parameter t satisfying the resolvent cubic equation:

$$t^3 - \frac{p}{2}t^2 - r_0 t + \frac{pr_0}{2} - \frac{q^2}{8} = 0.$$

Let t_0 be one real root of this cubic equation, and then the four solutions of the depressed quartic are:

$$y = \frac{1}{2}\left(\varepsilon_1\sqrt{2t_0 - p} + \varepsilon_2\sqrt{-2t_0 - p - \varepsilon_1\frac{2q}{\sqrt{2t_0 - p}}}\right), \quad \varepsilon_1, \varepsilon_2 \in \{+1, -1\}.$$

Therefore, $x = y - \dfrac{\tilde{b}}{4\tilde{a}}$.

To obtain a fully explicit form, the root t_0 of the resolvent cubic needs to be expressed in terms of radicals. For a general cubic equation

$$t^3 + \tilde{\alpha}t^2 + \tilde{\beta}t + \tilde{\gamma} = 0$$

with $\tilde{\alpha} = -\dfrac{p}{2}, \tilde{\beta} = -r_0$, and $\tilde{\gamma} = \dfrac{pr_0}{2} - \dfrac{q^2}{8}$, we set

$$\bar{p} = \tilde{\beta} - \frac{\tilde{\alpha}^2}{3}, \qquad \bar{q} = \frac{2\tilde{\alpha}^3}{27} - \frac{\tilde{\alpha}\tilde{\beta}}{3} + \tilde{\gamma},$$

and then one real root is

$$t = \sqrt[3]{-\frac{\bar{q}}{2} + \sqrt{\frac{\bar{q}^2}{4} + \frac{\bar{p}^3}{27}}} + \sqrt[3]{-\frac{\bar{q}}{2} - \sqrt{\frac{\bar{q}^2}{4} + \frac{\bar{p}^3}{27}}} - \frac{\tilde{\alpha}}{3}.$$



AIMS Press

© 2026 the Author(s), licensee AIMS Press. This is an open access article distributed under the terms of the Creative Commons Attribution License (https://creativecommons.org/licenses/by/4.0)